NUMERICAL MODELING OF THE LARGE-SCALE DYNAMICS OF INTERNAL WAVES

David Rubenstein

Science Applications International Corp.
PO Box 1303, McLean, VA 22102

ABSTRACT

Several issues related to large-scale modeling of internal waves are discussed. First, we consider the question of the linear internal wave response of the ocean to surface forcing. Past attempts at analyzing the linear response are briefly reviewed. Then we discuss a numerical experiment, in which a nonlinear model of internal waves generates a time-evolving field of motions in a vertical plane. The model flow is initially at rest, and is forced with a simple surface-layer body force with a long (40 km) wavelength. Despite the fact that the model was not initialized with a particular spectrum, it develops a frequency-wavenumber spectrum with features that are similar to that of Garrett and Munk. After a saturated spectrum develops, the dispersion of a cloud of Lagrangian tracer particles is analyzed. The linear dimensions of the cloud expand roughly as the square root of time. Based on the expansion rate we estimate values for eddy diffusivity coefficients. We find that these coefficients are independent of length scale, but vary approximately linearly with the internal wave horizontal kinetic energy. For a kinetic energy level equivalent to that of the Garrett-Munk spectrum and a stratification N~3 cph, we calculate K_x~0.26 m^2/sec, K_z~2×10^{-4} m^2/sec.

1. INTRODUCTION

Near-inertial waves are the most energetic component of the internal wave spectrum. Therefore it seems natural to focus (at least initially) on near-inertial waves, to understand their generation, dynamics, interactions, and dissipation. Near-inertial internal waves have rather long horizontal length scales (100's of meters to 10's of kilometers) in comparison with higher frequency waves. Therefore a numerical model of near-inertial waves should span this broad range of length scales.

The problem is even more difficult than this. Surface forcing of near-inertial waves due to atmospheric events covers an even broader range of length scales—up to 100's of kilometers. Certainly a wide variety of mesoscale, upper surface-layer and bottom boundary layer processes interact with near-inertial waves in this regime of spatial scales. Therefore it is important to try to sort out the relative magnitudes of all of the different interactions.

My overall objectives are to try to answer three important questions: 1) How are large-scale internal waves generated? 2) Once they are generated, how are their space and time scales maintained? 3) How do these waves interact with, and contribute to the mixing of, mesoscale flows?

Because the questions are still largely unanswered, I am following a multi-pronged approach. The first approach, discussed in Section 2, is to determine the extent to which linear dynamics are capable of generating the internal wave spectrum. A body of circumstantial evidence indicates that many of the characteristics of the internal wave field can be explained using linear mechanisms. The next approach, discussed in Section 3, is to determine whether wave-wave interactions are

sufficient to generate the internal wave spectrum, and over what time scales does such a spectrum develop and decay. Then results of some experiments related to the mixing of a passive tracer are presented in Section 4. The space-plus-time trajectories of Lagrangian tracer particles are calculated, and give us some insights into the mixing process.

2. LINEAR DYNAMICS OF GENERATION

It is known that wind-forcing is an important generator of near-inertial motions. Simple linear models of wind-induced inertial motions are sometimes able to explain a very large percentage of the inertial energy in the surface mixed layer. Sometimes these models fail in their deterministic predictions, for a variety of reasons. The reasons may include, for example, incomplete knowledge of the full wind field (its history and its spatial scales), mesoscale motions which interact with the inertial motions, inertial waves which have propagated from a distant source, and so on.

An important question which arises is, to what extent can *linear* dynamics explain the generation of near-inertial waves, and perhaps, the generation of the *entire* spectrum of internal waves. As far as near-inertial waves are concerned, there is a body of evidence that linear dynamics are sufficient. For example, Rubenstein (1983) showed that observed features related to vertical phase propagation and interchange of energy between the surface layer and the thermocline can be explained with linear dynamics. Kundu and Thomson (1985) showed that linear theory can explain the observed intermittency of near-inertial waves, and the horizontal phase structure of surface-layer oscillations. Gill (1984) presented a linear theory which explained many other features of near-inertial waves, such as the tendency for horizontal and vertical scales to decrease after a storm has passed. Eriksen (1988) examined the linear response of near-inertial waves to a wind stress which deposits a body force as a step function in the vertical; uniformly within a surface layer, and zero below. He found that the vertical wavenumber spectral response is the same as that predicted by the GM81 empirical spectrum.

In a sense, our understanding of the vertical scales of internal waves is much better than that of the horizontal scales. High-quality vertical profiles are easier to produce than horizontal profiles—especially profiles of velocity. Also, there are major gaps in our 2D+time description of the wind stress field. There have been several attempts to jump over these gaps.

Several years ago I performed a little study, in which I looked at the patterns of near-inertial motions generated in the surface layer. I digitized a couple of months of 6-hr synoptic weather maps in a 2600-km square region of the North Atlantic, roughly from 35°N to 60°N, and from 15°W to 50°W. I gridded the isobars and computed the geostrophic wind, adjusted for friction and for turning effects. Figure 1 shows an example of one such map. I used a very simple slab model for the mixed layer (uncoupled in the horizontal), and observed the patterns of near-inertial oscillations. Figure 2 shows a single snapshot of the u-component of velocity, after 40 days of evolution. There seems to be a notable difference between the northern and southern regions of the model domain. The northern half is dominated by propagating low-pressure systems. The wave pattern orientations and length scales are variable, on synoptic time scales. In contrast, the southern half of the model domain is dominated by a climatological high pressure system. As a result, the wave pattern is more static. The wave patterns tend to be elongated along latitude lines, because of the beta effect.

D'Asaro (1989) used an imaginative technique to bridge the wind-field problem. He used a Seasat scatterometer wind stress field, with 25-km resolution, and advected the field across the modeled

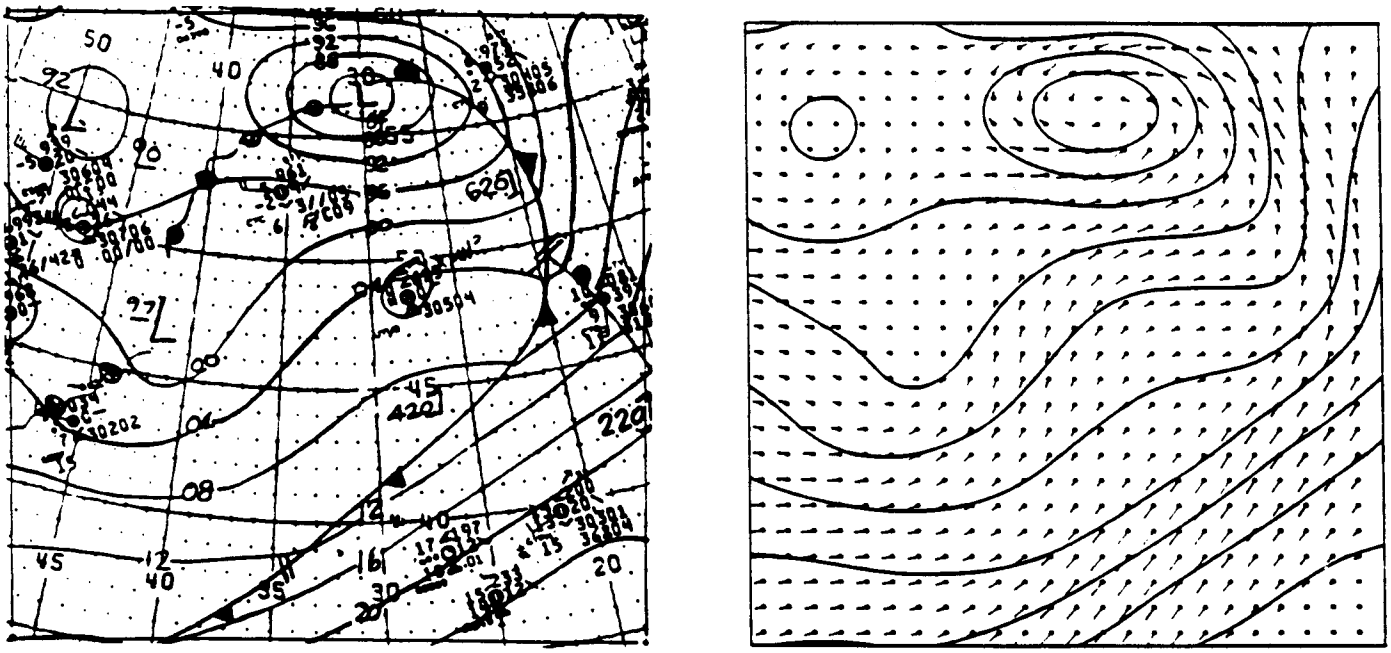

Figure 1. Left panel: Sample weather map over central North Atlantic. Right panel: Digitized, contoured isobars, and geostrophic wind adjusted for friction and turning effects.

ocean. In this way he was able to estimate the relative contributions of the wind field, the advection speed, and the beta effect, in generating smaller horizontal scales of near-inertial waves.

The problem with these approaches is that mesoscale and smaller-scale variance in the wind stress field is deficient. I've been developing a possible remedy to this problem. The approach is to start with an atmospheric mesoscale model, and to perform a stochastic interpolation in time and space, to resolve higher wavenumbers and frequencies. This is a sort of engineering approach, but if it yields a statistically realistic evolving wind field, it could give meaningful results.

3. NONLINEAR MODEL

If we apply an intermittent, large-horizontal-scale wind-induced surface forcing to a nonlinear model, what sort of internal wave spectrum develops? Over what time scale does such a spectrum develop, and after forcing is removed, over what time scale does it dissipate?

In an attempt to answer these questions, we formulate a two-dimensional model in a vertical x-z plane. Motion is allowed in three directions, but the model is invariant in the y-direction. We assume an initially motionless ocean, with an exponentially decaying buoyancy frequency, and a fluid which satisfies the Boussinesq approximation. The lateral, top and bottom boundary conditions are reflecting.

The coordinates (x,y,z) are defined with z positive upward, with the origin at the ocean bottom. A channel of depth D=1 km (corresponding to a flat ocean bottom) and width X=20 km contains the flow. The equations of motion are

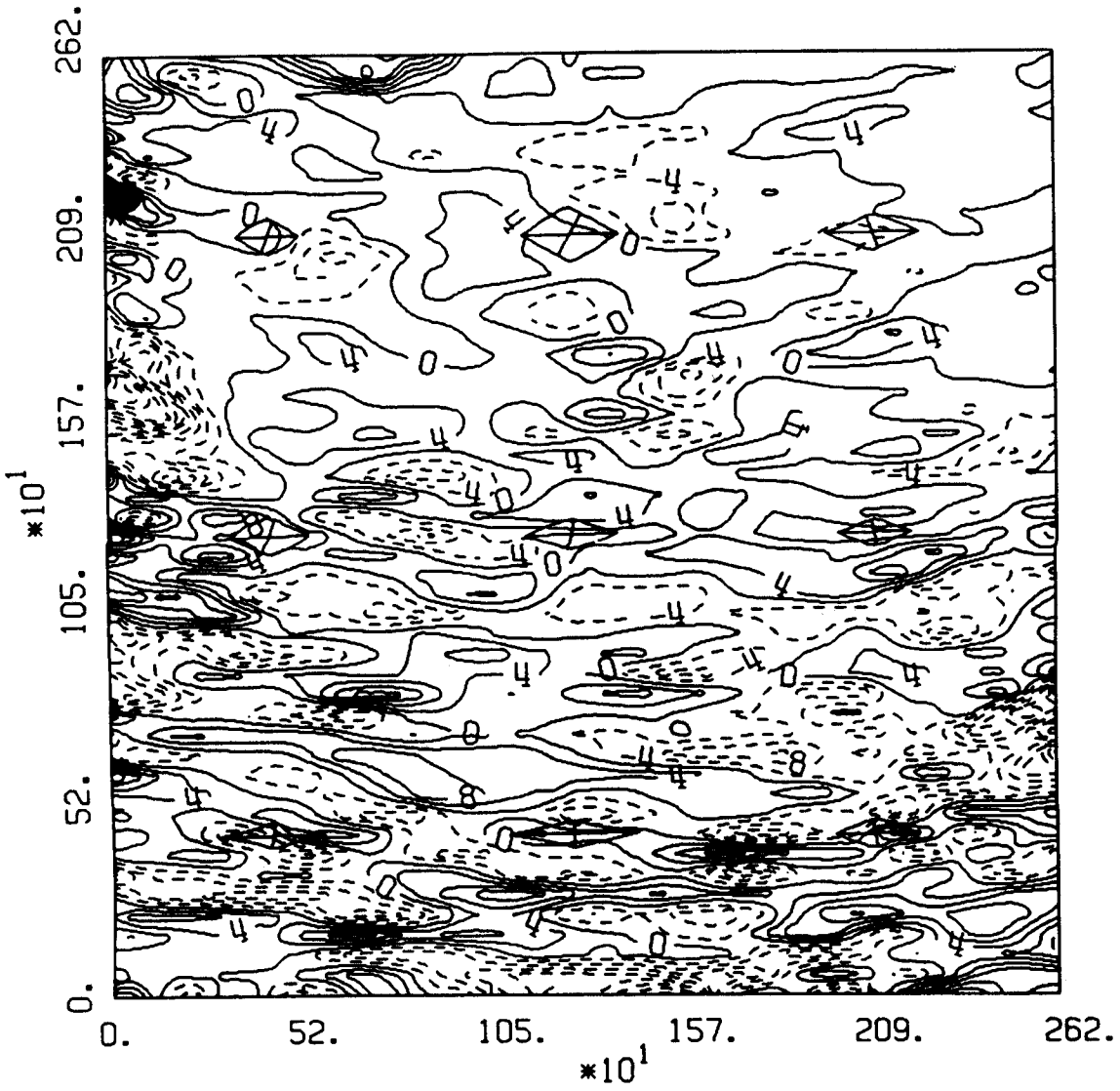

Figure 2. U-component of velocity in the surface layer, predicted by a simple slab model. The spatial domain is a 2,620 km square region, as shown in Fig. 1. The contour interval is 4 cm/sec. The elongation of structures along latitude lines is due to the beta-effect. The longer length scales in the northern half of the domain is due to the rapid, successive propagation of atmospheric fronts.

$$\partial_t u + u\partial_x u + w\partial_z u - fv = -\partial_x p + \kappa_x \partial_{xx} u + \kappa_z \partial_{zz} u + F \tag{1}$$

$$\partial_t v + u\partial_x v + w\partial_z v + fu = + \kappa_x \partial_{xx} v + \kappa_z \partial_{zz} v \tag{2}$$

$$\partial_t b + u\partial_x b + w\partial_z b + N^2 w = + \kappa_x \partial_{xx} b + \kappa_z \partial_{zz} (b + B) \tag{3}$$

$$\frac{\partial u}{\partial x} + \frac{\partial w}{\partial z} = 0 \tag{4}$$

$$\frac{\partial p}{\partial z} = b \tag{5}$$

$$N^2 = \frac{\partial B}{\partial z}, \quad B_T = B + b \tag{6}$$

The velocity components are (u, v, w), p is a reduced perturbation pressure, $N=(3\ \text{cph})\times e^{-z/1300}$ is the buoyancy frequency profile, and f is the Coriolis parameter. The total buoyancy B_T is split up into a steady, initial profile $B(z)$ and a perturbation buoyancy b. The κ_x and κ_z terms are diffusivity coefficients, and are uniform in space. A rigid lid leads to an additional constraint, that

$$\int_0^D u\,dz = 0 \tag{7}$$

The model is driven by a body force distributed in the surface layer of depth H. The body force has a single, large-scale horizontal sinusoidal component, and is given by

$$F(x,z,t) = F(t)\sin(\frac{\pi x}{X})\,\frac{1}{2}[1+\sin(\pi\frac{z-(D-H)}{2H})]\ . \tag{8}$$

The behavior of $F(t)$ simulates a short-duration impulse. During an initial spinup period, these impulses were applied at regular intervals of 5.5 inertial periods. After the wavenumber spectrum is saturated, the forcing is turned off, and the flow is allowed to decay.

The diffusion coefficients κ_x and κ_z are chosen to have the minimum possible values, and still maintain numerical stability. During the spinup period, we set κ_x=0.1 m^2/sec and κ_z=10^{-4} m^2/sec, and during the decay period we set κ_x=0.05 m^2/sec and κ_z=5×10^{-5} m^2/sec. We find that during the decay period, energy dissipates with an e-folding time scale of about 30 days. This time scale falls within the 15-44 days time scale estimated for the replenishment of the internal wave field (Gregg, 1987).

Spatial derivatives are approximated by centered differences, and time integration is performed using the two-step Lax Wendroff technique. The finite difference equations are solved on a 128×128 grid, using a time step of 12 seconds. The artificial viscosity associated with this numerical technique is given by (Roache, 1972)

$$\kappa_{art} = u^2\,\Delta t/2\ . \tag{9}$$

In the model runs presented here, this artificial viscosity is less than a quarter of the explicit diffusion coefficients, in both the horizontal and the vertical.

Figure 3 shows spectra of kinetic energy in two projections; ω-k_x and ω-k_z, where ω is frequency, k_x is horizontal wavenumber, and k_z is vertical wavenumber. We first consider the ω-k_z spectrum. The strongest ridge parallel to the k_z axis corresponds to near-inertial waves. The next-strongest

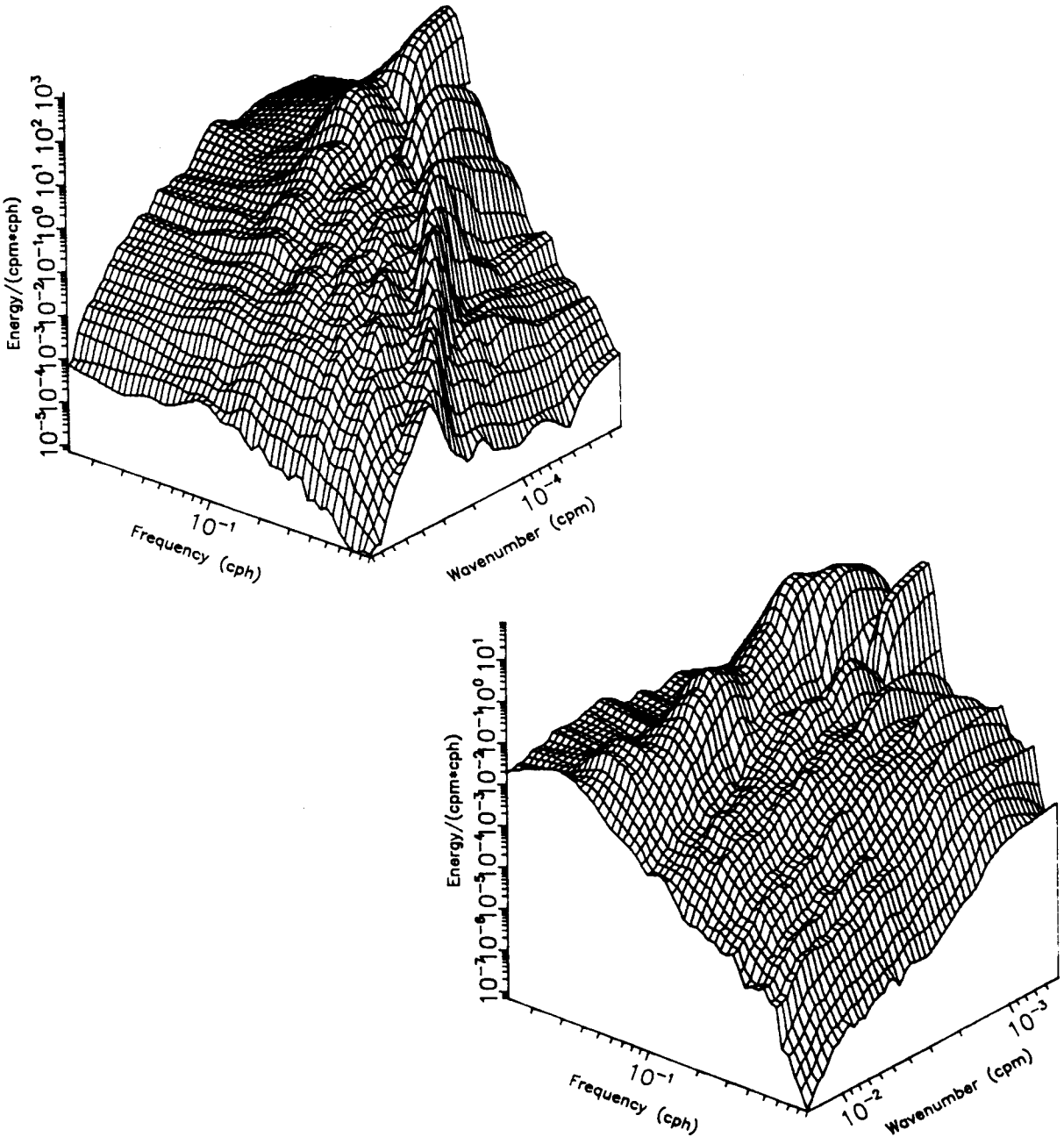

Figure 3. Kinetic energy spectrum, predicted by the nonlinear numerical model. The top panel shows a projection in ω-k_x space, and the bottom panel shows ω-k_z.

ridge, at a slightly higher frequency, corresponds to the first vertical mode. The weaker, higher-frequency ridges correspond to harmonics. In the ω-k_x spectrum, we see some of the same features, but in addition we see a set of radial ridges. The radial ridges are the projections of discrete vertical modes onto the ω-k_x spectrum.

It is also interesting to note that the ω-k_z spectrum appears to be nearly (but not exactly) separable between ω and k_z, while the ω-k_x spectrum is not remotely separable in ω and k_x. This feature of separability in ω-k_z and non-separability in ω-k_x is similar to that of the Garrett-Munk spectrum (for example, Munk, 1981). The feature is somewhat at odds with the slant-wavenumber frequency spectrum observed by Pinkel (1984). Pinkel's wavenumber spectra in the upper ocean exhibit slopes which flatten with increasing frequency.

On the other hand, both the modeled ω-k_z spectrum and Pinkel's (1984) observed spectrum show a set of ridges parallel to the k_z axis. In the case of the model, these ridges represent harmonics between the lowest vertical modes of the near-inertial frequency waves. In the case of Pinkel's observations, these ridges represent possible harmonics between tidal and inertial frequency motions. In both model and observations, these ridges stand out at low wavenumber, but not at high wavenumber.

4. DISPERSION OF LAGRANGIAN TRACER PARTICLES

Eddy viscosity and diffusivity coefficients are employed by ocean circulation models, for the purpose of parameterizing sub-grid scale mixing processes. Much of this sub-grid scale mixing is due to the internal wave field. Several techniques have been developed for the estimation of diffusivities. Direct observations of internal waves (Ruddick and Joyce, 1979; Brown and Owens, 1981; Kunze, 1986; Hebert, 1987) use the eddy correlation technique to derive eddy viscosity and diffusivity. Sometimes even the sign of the derived viscosity or diffusivity coefficients is in doubt. These direct observations are limited because in the thermocline, eddy correlation signals are weak, and they are disturbed by non-stationarity of the mean flow.

Other techniques for estimating viscosity and diffusivity parameters are extensively reviewed by Gregg (1987). These techniques include inverse methods over regional domains, flux estimations from microstructure measurements, compilations of statistics of mixing patches, and direct measurements of dye patches (Ewart and Bendiner, 1981; Ledwell, 1989).

One technique that has not yet received much attention is numerical simulations. Numerical simulations have the advantage that they are capable of separating the diffusion due to internal waves from that of mesoscale motions. They also allow sensitivity studies to systematic parameter variations, and of course, allow complete understanding of the underlying flow field. On the other hand, full nonlinear models have the significant disadvantage of covering a limited range of length scales. Another limitation is the lack of direct control over the spectral level and shape.

To help understand mixing due to internal waves, we consider the dynamics of Lagrangian particles. Figure 4 shows the trajectories of nine individual Lagrangian particles over an 8-day interval. The particles are tracked between the grid cells using bilinear interpolation. The horizontal extents Δx of the tracer trajectories are on the order of 1 to 4 km, and the vertical extents Δz range from 30 to 80 m.

We are not interested only in the absolute dispersion of a tracer particle; we are interested in the *relative* dispersion of a cluster of particles. The four panels in Figure 5 show the positions of 1000 tracer particles at four instances in time; 1.6, 3.3, 6.6, and 11.6 days. The thick circle in each panel (actually an ellipse in physical space; major axis=312 m in the horizontal, minor axis=15.6 m in the vertical) indicates the initial distribution of the particles. In each panel, the portrayed positions of the particle clouds have been translated to keep the centers of mass coincident with the centers of the panels. At the early times, the particles remain organized in stringy clumps. At the later times, the particles separate from one another, and their positions become more random.

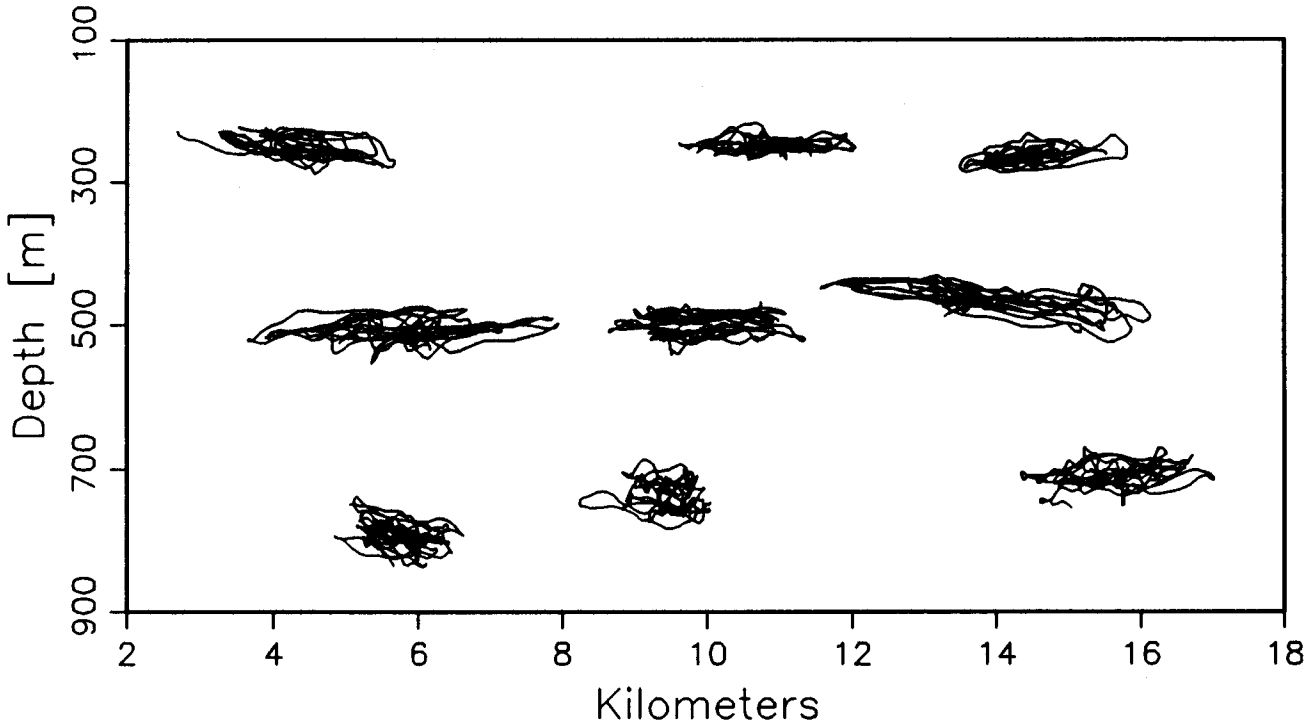

Figure 4. Trajectories of nine individual Lagrangian particles in a vertical plane, due to modeled internal waves over an 8-day interval when the model was quite energetic.

In each panel, a thin-line ellipse is drawn to indicate the standard deviation of the particle distribution in two orthogonal directions. The size of the ellipse tends to increase with time. By 11.6 days, the ellipse has increased by a factor of 5.5 relative to its initial size. The eccentricity does not have a noticeable trend with time.

To obtain a statistical average, we constructed a hierarchical grid of clouds of Lagrangian particles. A 5×5 grid of cloud centers was placed in the central area of the model domain. These clouds were initially circular in the finite grid space, and therefore elliptical in physical space. A hierarchy of 5 initial cloud sizes allowed a larger range of spatial scales to be examined. We traced the trajectory of each particle, and computed the ensemble average variance of the cloud distributions (segregated by initial cloud size) in the horizontal and vertical directions.

Figure 6 shows the average cloud distribution variances in the horizontal and vertical directions. Both panels in the figure show a set of five curves, each corresponding to a different initial cloud radius. The thin, oscillating curves represent the ensemble-averaged distribution variances, and the thick, smooth curves represent low-pass filtered time series, with a 1-day time constant. For the first 8 days, the variance increases approximately linearly with time. From this rate of increase, we can estimate the effective eddy diffusion coefficients in the horizontal and in the vertical,

$$K_x = \frac{1}{2}\frac{d\sigma_x^2}{dt} \approx 0.7\ \mathrm{m^2/sec}\ , \qquad (10)$$

$$K_z = \frac{1}{2}\frac{d\sigma_z^2}{dt} \approx 5\times10^{-4}\ \mathrm{m^2/sec}\ .$$

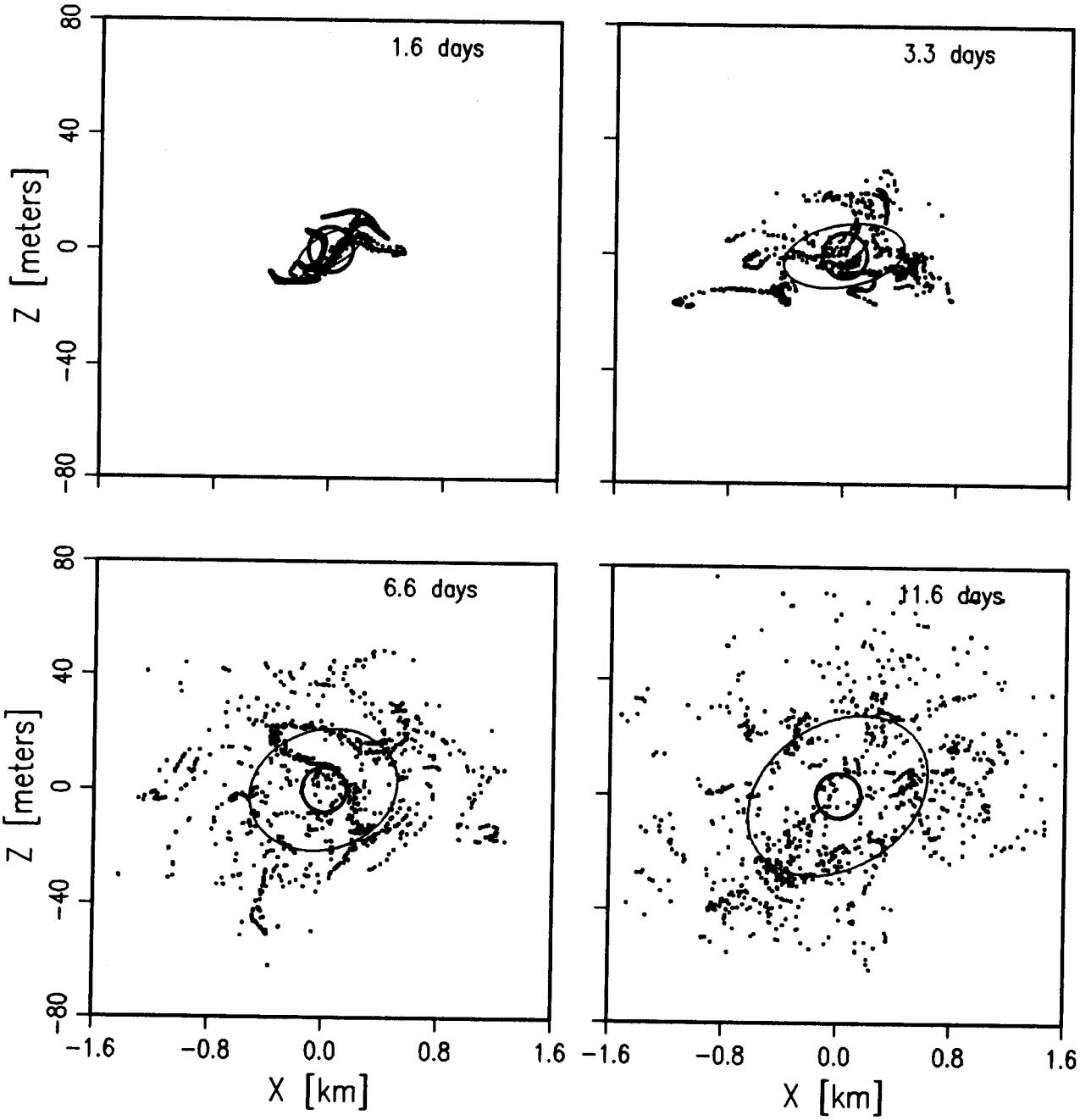

Figure 5. Relative dispersion of 1000 tracer particles in a vertical plane at four instants in time; 1.6, 3.3, 6.6, and 11.6 days. The thick curve in each panel (appears as a circle in this compressed coordinate space) is the locus of the initial distribution of particles. The thin-line ellipse in each panel indicates the standard deviation of particle distribution, in two orthogonal directions.

After 8 days, the variance increases more slowly (K_x~0.3 m^2/sec, K_z~3x10^{-4} m^2/sec). This occurs because kinetic energy is slowly dissipating (the rms u-component of velocity has decreased from 7.5 to 6 cm/sec), and the rate of expansion of the cloud size is very sensitive to the kinetic energy spectrum.

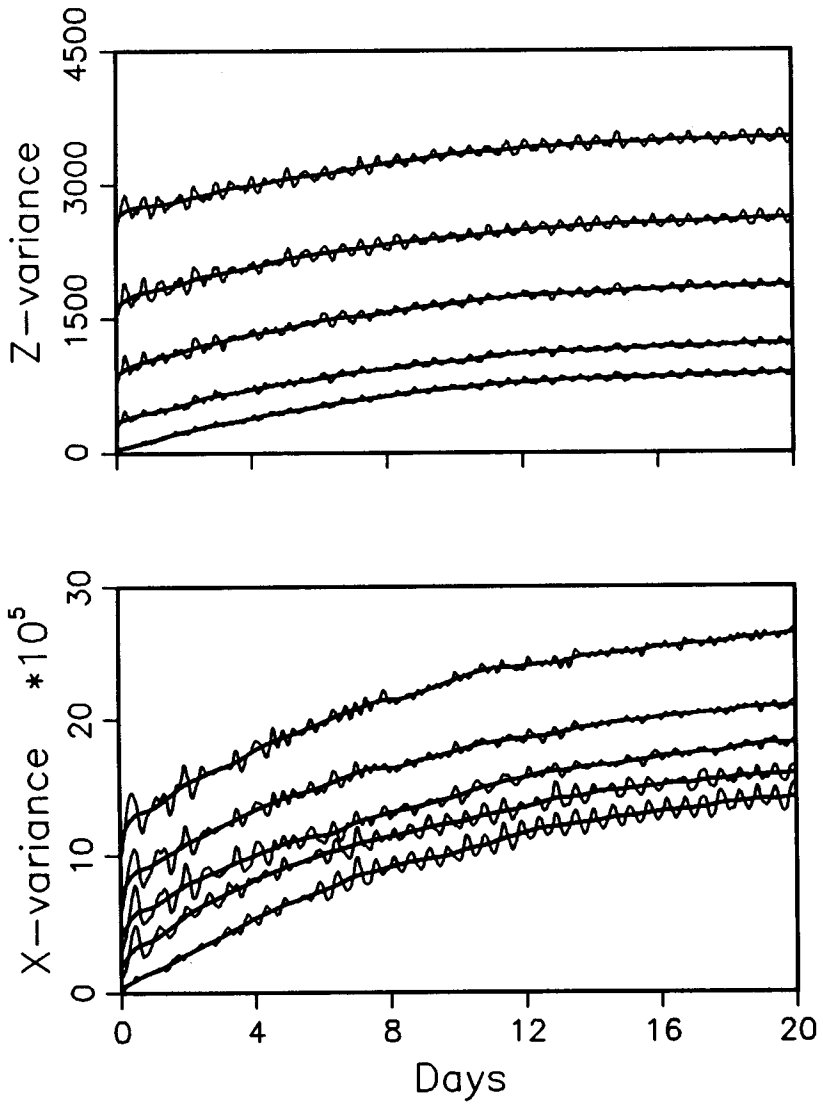

Figure 6. Thin curves: Ensemble average tracer cloud distribution variances in the horizontal and vertical directions. Thick curves: Time-average (1 day time constant) which smooths out the oscillations due to isopycnal deformations.

Despite the gradual decrease in expansion rate of the tracer clouds, the distribution variances for the various initial cloud sizes are all parallel to one another. The implication is that although the rates of increase $d\sigma_x^2/dt$ and $d\sigma_z^2/dt$ are sensitive to the kinetic energy spectrum, they are independent of σ_x^2 and σ_z^2. In other words, the effective eddy diffusivities are independent of the length scales involved. This result is in contrast with Okubo's (1971) finding that horizontal diffusivity increases with length scale to the 1.1 power. We must keep in mind that the observations compiled by Okubo include the effects of the entire, complicated spectrum of ocean velocities. The numerical prediction that eddy diffusivity is independent of length scale is largely due to the facts that only internal wave motions are included, and that tracer cloud length scales fall within the internal wave spectral continuum, which has a rather constant slope over a wide range of wavenumbers.

The short term oscillations in Fig. 6 represent deformations of the tracer clouds, associated with isopycnal straining and tilting. The ensemble average over sets of independent tracer clouds has removed a portion of the isopycnal deformations. The time-averaged, smooth curves have removed the residual deformations, and represent true diapycnal (across density contours) and isopycnal (along density contours) mixing.

Horizontal and vertical diffusion coefficients are plotted in Figure 7, as a function of rms horizontal velocity. These coefficients were estimated at different times during the model integration, as the energy level dissipated. Best fitting quadratic coefficients were estimated;

$$K_x = 54\,\sigma_u^2\,, \qquad K_z = 0.042\,\sigma_u^2\,, \tag{11}$$

where σ_u is the rms horizontal velocity. At the buoyancy frequency N=3 cph, the Garrett-Munk spectral energy level yields σ_u~7 cm/sec, and from Eq. (11) we get K_x~0.26 m^2/sec and K_z~2×10^{-4} m^2/sec. A quadratic fit of K_x and K_z to σ_u seems to be reasonable; therefore the eddy diffusion coefficients vary approximately linearly with horizontal kinetic energy.

The results of this study can be compared with recent measurements of ocean tracers. Ledwell (1989) measured the diapycnal spreading rate of a tracer, and deduced an approximate value K_z~3×10^{-5} m^2/sec, in the Santa Monica Basin. During the experiment, the buoyancy frequency was about 1 cph, and the rms internal wave velocity (excluding the low-mode, semidiurnal internal tide component) was approximately σ_u=3 cm/sec. Substituting this value into Eq. (11), we get K_z=3.8×10^{-5} m^2/sec, in good agreement with the measured value.

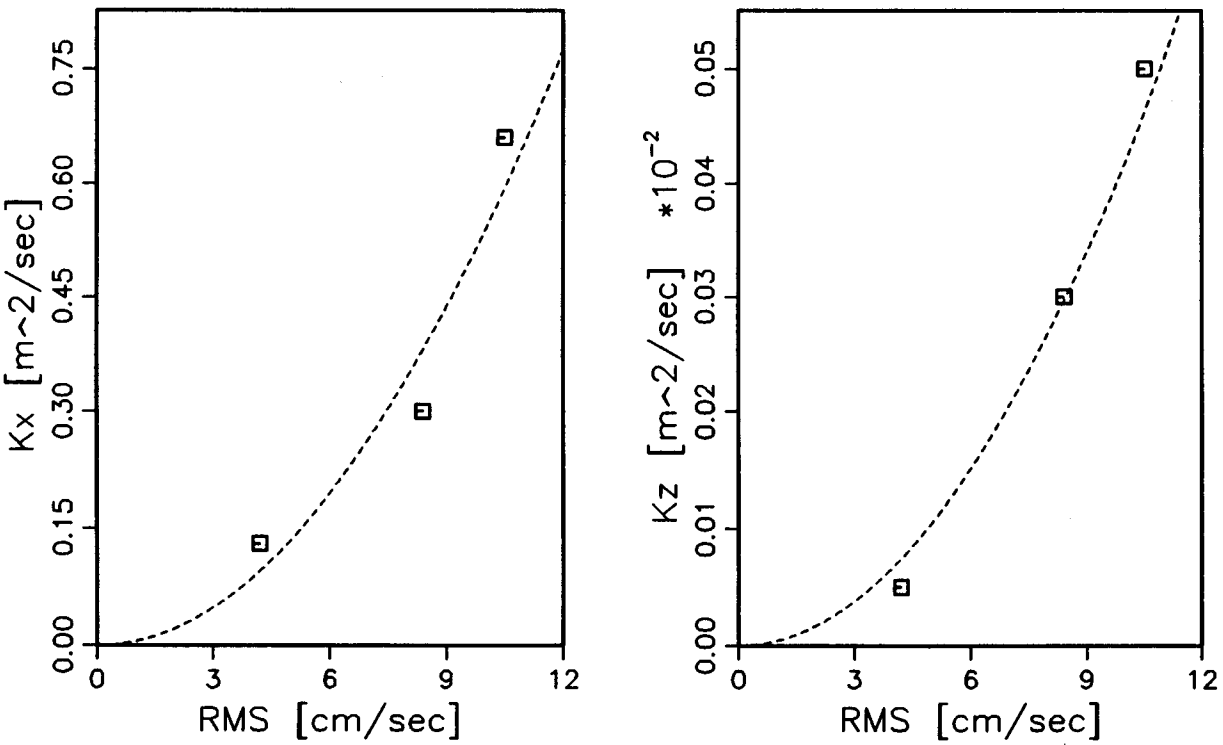

Figure 7. Horizontal and vertical diffusion coefficients, as a function of rms horizontal velocity associated with internal waves.

In another dye spreading experiment performed by Ewart and Bendiner (1981), several types of diffusion were computed. Assuming Fickian diffusion, estimates for K_x ranged from 0.03 to 0.12 m^2/sec. A local estimate of $K_z \sim 10^{-6}$ m^2/sec was observed associated with edge gradients, and a global value of about 5×10^{-5} m^2/sec was associated with total patch thickness. Assuming a Garrett-Munk energy level at $N=1$ cph, these estimates should be compared with model predictions of $K_x=0.08$ m^2/sec and $K_z=7 \times 10^{-5}$ m^2/sec.

The randomization of particle positions shown in Fig. 5 implies that the perimeters of the particle clouds become increasingly convoluted with time. Figure 8 shows the perimeters of four clouds of particles, initially concentric ellipses. The length scales eventually become shorter than the grid cell resolution. Even though the perimeter of a tracer cloud becomes increasingly convoluted with time, the buoyancy field does not. As soon as a buoyancy field kink develops to a sufficiently short scale, the explicit diffusivity parameterization in Eqs. (1)-(3) smooths the kink out. In this way the tracer particles, which are not directly affected by the explicit diffusivity, become disassociated from any specific isopycnal surface. Strong internal wave motions generate these "kinks" more rapidly than do weak motions, and therefore diapycnal mixing is more rapid. The exact values of the explicit coefficients κ_x and κ_z are not critical to the effective eddy diffusivities. In an experiment where κ_x and κ_z were doubled in value, the energy level decayed more rapidly, so the effective eddy diffusivities K_x and K_z likewise decreased in magnitude.

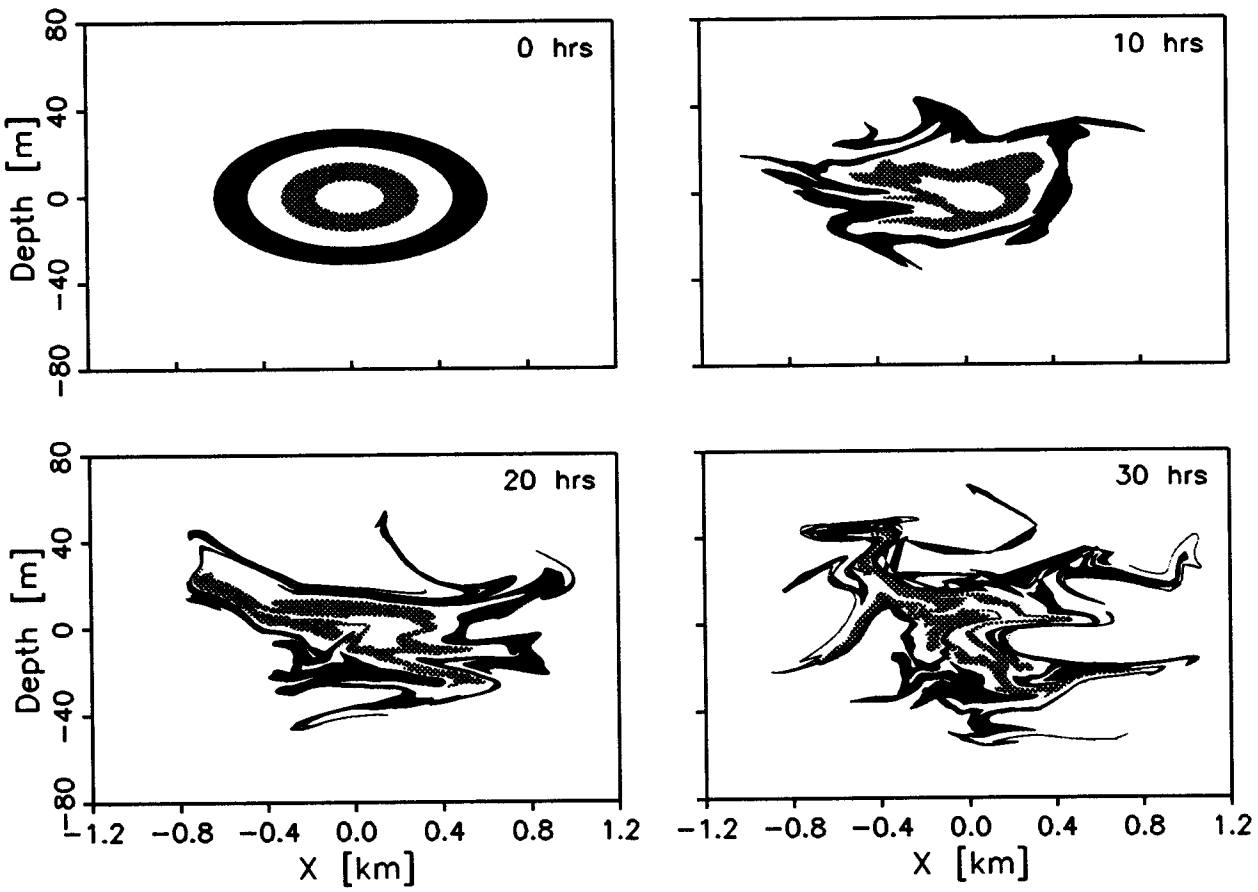

Figure 8. Four clouds of tracer particles were released into the numerical model, in initial concentric elliptical distributions. The outlines of these clouds are indicated by the inner and outer perimeters of the shaded areas.

In order to attain physical intuition into the diffusion mechanism, Young et al. (1982) developed analytic models of advection-diffusion. Young et al. modeled cases where a vertically sheared horizontal velocity field advects a tracer. Given tracer diffusivities κ_x and κ_z, an additional effective horizontal diffusivity K_x develops due to the interaction of the vertical shear and κ_z. They assumed a value of $\kappa_z \sim 10^{-5}$ m^2/sec, and for a particular model shear spectrum derived

$$K_x - \kappa_x \approx 1300\,\kappa_z \approx 0.013\ \text{m}^2/\text{sec} \tag{12}$$

The physical mechanisms incorporated into the numerical model are different from those analyzed by Young et al. (1982). The numerical model explicitly includes vertical velocities, and implicitly develops an effective vertical diffusivity K_z. If we were simply to substitute the value of the diffusion coefficient $\kappa_z = 5\times10^{-5}$ m^2/sec—which was used in Eqs. (1-3)—into Eq. (12), then we would obtain an effective diffusivity K_x much smaller than numerically computed values. On the other hand, if we combine the expressions in Eq. (11), we get the relationship

$$K_x = 54/0.042\,K_z = 1286\,K_z\ . \tag{13}$$

If we acknowledge that nonuniform, nonstationary vertical velocities in the numerical model generate an effective eddy diffusivity K_z in addition to κ_z, then we see that the results expressed in Eqs. (12) and (13) are quite comparable.

ACKNOWLEDGMENTS: This work is a result of research sponsored by the Office of Naval Research, under Contract N00014-88-C-0225. Thanks go to Michael Brill and David Bacon for stimulating discussions from which this study benefitted.

REFERENCES

Brown, E.D., and W.B. Owens, 1981: Observations of the horizontal interactions between the internal wavefield and the mesoscale flow. *J. Phys. Oceanogr.*, **11,** 1474-1480.

D'Asaro, E.A., 1989: The decay of wind-forced mixed layer inertial oscillations due to the ß effect. *J. Geophys. Res.*, **94,** 2045-2056.

Eriksen, C.C., 1988: On wind forcing and observed oceanic wave number spectra. *J. Geophys. Res.*, **93,** 4985-4992.

Ewart, T.E., and W.P. Bendiner, 1981: An observation of the horizontal and vertical diffusion of a passive tracer in the deep ocean. *J. Geophys. Res.*, **86,** 10,974-10,982.

Gill, A.E., 1984: On the behavior of internal waves in the wakes of storms. *J. Phys. Oceanogr.*, **14,** 1129-1151.

Gregg, M.C., 1987: Diapycnal mixing in the thermocline: A review. *J. Geophys. Res.*, **92,** 5249-5286.

Hebert, D., 1987: An estimate of the effective horizontal eddy viscosity in the Gulf Stream due to internal waves. *J. Phys. Oceanogr.*, **17,** 1837-1841.

Kundu, P.K. and R.E. Thomson, 1985: Inertial oscillations due to a moving front. *J. Phys. Oceanogr.*, **15,** 1076-1084.

Kunze, E., 1986: The mean and near-inertial wave velocity fields in a warm-core ring. *J. Phys. Oceanogr.*, **16,** 1444-1461.

Ledwell, J.R., 1989: A strategy for open ocean mixing experiments. *Parameterization of Small-Scale Processes,* Proceedings Hawaiian Winter Workshop, Univ. of Hawaii, P. Muller and D. Henderson, Eds., pp. 157-163.

Munk, W.H., 1981: Internal waves and small scale processes. *Evolution of Physical Oceanography,* B.A. Warren and C. Wunsch, Eds., The MIT Press, 264-290.

Okubo, A., 1971: Oceanic diffusion diagrams. *Deep-Sea Res.,* **18,** 789-802.

Pinkel, R., 1984: Doppler sonar observations of internal waves: The wavenumber frequency spectrum. *J. Phys. Oceanogr.,* **14,** 1249-1270.

Roache, P.J., 1972: On Artificial Viscosity. *J. Computational Physics,* **10,** 169-184.

Rubenstein, D., 1983: Vertical dispersion of inertial waves in the upper ocean. *J. Geophys. Res.,* **88,** 4368-4380.

Ruddick, B.R., and T.M. Joyce, 1979: Observations of interaction between the internal wavefield and low-frequency flows in the North Atlantic. *J. Phys. Oceanogr.,* **9,** 498-517.

Young, W.R., P.B. Rhines, and C.J.R. Garrett, 1982: Shear-flow dispersion, internal waves and horizontal mixing in the ocean. *J. Phys. Oceanogr.,* **12,** 515-527.